

1 **Rational design of Bi-doped rGO/Co₃O₄ nanohybrids**
2 **for ethanol sensing**

3 Sheng-Xun Cai ^{a†}, Xian-Qiang Song ^{a†}, Zong-Tao Chi ^a, Yong-Qing Fu ^b, Zheng-Tao Fang ^a, Sun-Ying-Yue Geng ^a,
4 Ya-Ru Kang ^a, Xiao-Xu Yang ^a, Jian-Feng Qin ^c, Wan-Feng Xie ^{a*}

5 ^a School of Electronics & Information, State Key Laboratory of Bio-Fibers and Eco-Textiles, Qingdao University,
6 Qingdao 266071, China

7 ^b Faculty of Engineering and Environment, Northumbria University, Newcastle upon Tyne NE1 8ST, UK

8 ^c Qingdao Open University, Qingdao 266071, China

9

10

11

12 * To whom correspondence should be referred.

13 Wan-Feng Xie: wfxie@qdu.edu.cn

14

15

16

17

18

19

20

21

22

23

24

25 **Abstract**

26 Gas sensors based on metal oxide semiconductors (MOSCs) and reduced graphene
27 oxide (rGO) for sensing of organic volatile compounds often suffer from high operation
28 temperature, low responses, poor selectivity, or narrow detection range. Herein, we
29 design and fabricate Bi-doped rGO/Co₃O₄ (BGCO) nanohybrids with a flower
30 morphology, which have been applied as a sensing layer for an ethanol sensor. This
31 BGCO sensor exhibits a maximum *p*-type response of 178.1 towards 500 ppm ethanol
32 at an optimum working temperature of 120 °C. The sensor's detection range for the
33 ethanol concentration is from 500 ppb to 500 ppm, and the sensor has an excellent
34 selectivity to ethanol compared to other types of organic volatile gases and oxidizing
35 gas such as NO₂. The enhanced ethanol sensing mechanism is attributed to the increased
36 conductivity of Bi doped rGO/Co₃O₄ material. Additionally, incorporation of Bi dopant
37 can promote the redox reaction, and the MOSCs act as the catalyst.

38 **Keywords:** semiconducting metal oxide, rGO, Bi doped Co₃O₄, ethanol sensor,
39 resistive sensor

40

41

42

43

44

45

46

47

48

49

50

51

52

53

54

55 **1. Introduction**

56 With the rapid development of Internet of things, various sensor-based techniques
57 are being extensively developed and applied for industry, agriculture, environment
58 control, enhancement of life quality, and safety [1-4]. Among various types of sensors,
59 chemiresistive gas sensors based on metal oxide semiconductors (MOSCs), such as
60 Co_3O_4 [5], $\text{rGO}/\text{Co}_3\text{O}_4$ [6-8], Bi_2O_3 [9], SnO_2 [10], In_2O_3 [11], and WO_3 [12,13], as
61 well as their nanocomposites [14-16], have many advantages including good sensitivity,
62 selectivity, stability, cost effectiveness, and simple implementation for real-time control.
63 All of these make them competitive for usages in environmental monitoring, food safety,
64 industrial production, and disease diagnosis [17-19].

65 Volatile organic compounds (VOCs), including ethanol ($\text{C}_2\text{H}_6\text{O}$), formaldehyde
66 (CH_2O), toluene (C_7H_8), methanol (CH_3OH), ethylene glycol ($(\text{CH}_2\text{OH})_2$) and other
67 aromatic carbohydrates, are hazardous to human health and can cause irritation of
68 mucous membranes and upper respiratory tracts [20,21]. Nevertheless, our olfactory
69 system is insensitive to accurately detect these types of harmful gases. Therefore, it is
70 critical to develop high performance gas sensors not only for detection of toxic,
71 explosive or flammable vapors (which could come from free emissions or destructive
72 leakage), but also for quality or concentration control of living conditions, traffic
73 routine inspections, rapid disease diagnosis and food inspection [22]. Ethanol
74 ($\text{CH}_3\text{CH}_2\text{OH}$), for example, is one of the important VOCs used in food, biological and
75 brewing industries. In recent years, studies for gas sensors for ethanol have been
76 increased rapidly due to their extensive applications such as drunken-driving
77 monitoring, safety tests for food package, and leakage detection in chemical factories
78 [23,24]. Large quantity leakage or evaporation of ethanol may induce risk of explosion
79 in brewery houses or storehouses [25]. Therefore, it is critically required for ethanol
80 sensors with low operating temperature, fast detection, high sensitivity, and good
81 selectivity.

82 The key working mechanism of these MOSCs based gas sensors is that the target gas
83 molecules are chemisorbed and react with the oxygen species such as O^- , O_2^- , O^{2-} on
84 the surface of the sensing material, which leads to changes of device's properties such

85 as electrical resistance [8,17]. To further enhance the gas sensing performance
86 including low working temperature, sensitivity, selectivity, stability, and reproducibility,
87 different strategies have been developed [26]. For example, doping of these MOSCs
88 have been extensively studied to enhance the synergistic effects of the binary/ternary
89 metal oxide materials (Bi_2O_3 , SnO_2 , MoO_3 and Co_3O_4) and increase the surface
90 chemical states of the electrons and high surface-to-volume ratios [27].
91 Heterostructures have also been widely used, including *n-n*, *p-p* and *p-n* junctions,
92 where *p* is *p*-type semiconductor, *n* refers to *n*-type semiconductor. Many studies also
93 applied composites of the MOSCs, for example, with the reduced graphene oxide (rGO),
94 which can manipulate the Fermi energy level and large specific surface area [28-30].

95 Recently, there are studies reported using $\text{Zn}_{1-x}\text{Fe}_x\text{O}/\text{rGO}$ [31], $\text{SnO}_2\text{-rGO}$ [32], rGO-
96 CuO [33] and $\text{MoO}_3\text{-rGO}$ [34] nanocomposites for the ethanol sensors. However,
97 $\text{rGO}/\text{Co}_3\text{O}_4$ [35], $\text{Co}_3\text{O}_4/\text{N-doped rGO}$ nanocomposites [8], and rGO decorated hollow
98 Co_3O_4 nano/microspheres [7], are still deserved to be further investigated due to their
99 low responses and high operating temperatures. For instance, Liu's group synthesized
100 rGO decorated hollow Co_3O_4 spheres using a solvothermal method and then applied
101 them into an ethanol sensor. The sensor showed a *p*-type sensing behavior, and the
102 response value is 13.5 towards 100 ppm ethanol, which is 3.7 times higher than that of
103 the pure Co_3O_4 [35]. In 2019, Sun's group fabricated Co_3O_4 and rGO nanosheets, which
104 have been used for ethanol sensing. They reported that the nanocomposite with 15 wt%
105 of rGO has the best sensitivity when operated at 200 °C [7]. In 2020, Lin and co-
106 workers reported that $\text{Co}_3\text{O}_4/\text{N-doped rGO}$ nanocomposite with a mesoporous structure
107 exhibited a *p*-type response for ethanol which can be operated at 200 °C [8].

108 In very recent years, various $\text{rGO}/\text{Co}_3\text{O}_4$ nanocomposites have been extensively
109 studied as the ethanol sensing materials. However, the sensor's performance such as
110 sensitivity, working temperature and selectivity of the $\text{rGO}/\text{Co}_3\text{O}_4$ based sensors is far
111 from satisfactory, owing to their relatively high intrinsic resistance. One alternative
112 strategy for enhancing sensing properties is to introduce other components (e.g., Bi, Zr,
113 Ag) [36-38], especially for those elements with a high electronegativity. These elements
114 can have a synergistic effect with Co to modulate the surface states, reactant adsorption,

115 and activation. According to the literature, the electronegativity of Bi is 1.9, which is
116 beneficial in gas sensing because it is known to promote electron transfer [39]. In
117 addition, the conductivity of Bi doped rGO/Co₃O₄ might be greatly improved because
118 of the mismatch of lattice constants [40], which was induced by the doped Bi, because
119 the radius of Bi atoms is larger than that of Co atoms. However, to the best of our
120 knowledge, there are few reports on the ethanol sensing using Bi-doped rGO/Co₃O₄
121 nanohybrids. Therefore, in the present investigation, Bi-doped rGO/Co₃O₄ nanohybrids
122 have been synthesized via one-pot solvent-thermal method. Based on this design
123 methodology, we found that incorporation of 1% Bi (mass ratio) into rGO/Co₃O₄
124 nanohybrid can enhance the ethanol sensing performance (e.g., response and selectivity)
125 significantly.

126 **2. Experimental**

127 2.1 Preparation of Bi-doped rGO/Co₃O₄ nanocomposite

128 All analytical grade reagents and chemicals were purchased from Aladdin (Shanghai,
129 China), and used as received without any further purification. Mixtures of 747.2 mg
130 Co(Ac)₂·4H₂O, 7.472 mg Bi(NO₃)₃·5H₂O, 500 mg 1,3,5 Trimesic acid (C₉H₆O₆), and
131 300 mg ammonium fluoride (NH₄F) were dissolved into the 40 ml absolute ethyl
132 alcohol, and obtained a solution A. Graphene oxide (GO) nanosheets were synthesized
133 from the natural graphite via the modified Hummers method, and then ultrasonically
134 dispersed into 10 ml absolute ethyl alcohol at 250 W for 2 h, which obtained a solution
135 B. Successively, the solutions of A and B were transferred into a 50 ml autoclave and
136 heated at 180 °C for 24 h. The obtained products were centrifugated and washed with
137 ethanol and water for 3 times, and dried at 80 °C for 12 h. The dark violet colored
138 precursor was changed into black powder after calcination at 300 °C for 2 h. According
139 to the mass ratio of Co(Ac)₂·4H₂O and Bi(NO₃)₃·5H₂O, the prepared Bi-doped
140 rGO/Co₃O₄ nanocomposite was denoted as 1%BGCO. Similarly, we prepared other
141 three samples via changing the weight of Bi(NO₃)₃·5H₂O from 0 mg (0%), 22.416 mg
142 (3%), to 44.832 mg (6%), and named them as 0%BGCO, 3%BGCO, and 6%BGCO,
143 respectively.

144

145 2.2 Preparation of gas sensing set-up

146 In the typical sensor fabrication process, 100 mg 0%BGCO, 1%BGCO, 3%BGCO,
147 6%BGCO nanocomposites were mixed with *N, N*-dimethylformamide (DMF) to form
148 paste, respectively. The paste was then drop-coated onto the surface of a ceramic tube
149 with four platinum (Pt) electrodes to form a uniform coating. The coated ceramic tube
150 with the BGCO were welded to a special six-polar pedestal. Finally, a Ni–Cr heating
151 coil was inserted into the coated ceramic tube for heating purposes. The gas sensing
152 performance was characterized using a gas sensing system (MA1.0, Narui Electronics
153 Co. Ltd., China). The sensing response was calculated by the resistance ratio of the
154 sensor resistance in sensing gases (R_g) to that in fresh air (R_a). The response time was
155 defined as the time taken for the 90%-fold resistance alteration of gas sensors in the
156 adsorption processes, whereas the recovery time was defined as the period taken by
157 sensing device to reach 90% of its initial resistance after the exposed to air [41].

158 2.3 Materials Characterization

159 X-ray diffraction (XRD) patterns of the composites were obtained using a Bruker
160 AXS (D8, advance, Cu $K\alpha$ X-ray source) diffractometer at a scanning rate of 1° min^{-1} .
161 The morphologies of the samples were investigated using a field emission scanning
162 electron microscope (FE-SEM, Zeiss Gemini 500) and a high resolution transmission
163 electron microscope (HR-TEM, JEOL-2100F 200 kV). The elemental mapping of the
164 samples was performed using an energy dispersive X-ray spectroscope (EDX, Oxford
165 Link-ISIS 300) at 15 kV. The spectra of X-ray photoelectron spectroscope (XPS) were
166 recorded using a Thermo Scientific Escalab 250xi instrument equipped with a
167 monochromatic Al $K\alpha$ source. The specific surface areas were determined by BET
168 measurements (Autosorb iQ Station 1, USA). Experiments using ultraviolet
169 photoelectron spectroscopy (UPS, Thermo Fisher Scientific Co.) was carried out in
170 ultrahigh-vacuum environment with He I ($h\nu = 21.2 \text{ eV}$).

171 3. Results and discussion

172 Fig. 1a presents the synthesis process of the BGCO sensing materials. Here, the
173 BGCO nanohybrids were obtained via one-pot solvent-thermal method. Fig. 1b shows
174 the surface morphologies and microstructures of the nanocomposite of Bi-doped

175 rGO/Co₃O₄ obtained using the FE-SEM. The surface of 1%BGCO composite shows a
176 flower-type morphology, and the lamellar structure of rGO could hardly be seen as the
177 substrate for the nucleation and growth of Co₃O₄. The surface also shows
178 interconnected pores, and the pore diameter is ranged from several nanometers to
179 several micrometers (Fig. 1c), which is consistent with the structure of the rGO [42].
180 Fig. 1d shows a TEM image, revealing the Co₃O₄ on the translucent layer of rGO [43].
181 Fig. 1e shows a HR-TEM image of the sample, where the two lattice fringes with
182 spacings of 0.47 nm and 0.24 nm are identified as the (111) and (311) lattice planes of
183 hexagonal Co₃O₄ [44,8]. To elucidate the elemental composition of the 1%BGCO
184 nanohybrids, EDX elemental mapping was performed (Fig. 1f to i), and the results
185 confirm that the sample of 1%BGCO contain C (Fig. 1f), O (Fig. 1g), Co (Fig. 1h) and
186 Bi (Fig. 1i), evenly distributed within the selected area. On the other hand, Bi elements
187 are sparsely scattered on the surface of 1%BGCO.

188

189

190 **Fig. 1.** (a) Illustration of the synthesis process of flower shaped Bi-doped rGO/Co₃O₄ nanohybrids; (b) low-
191 magnification SEM and (c) high-magnification SEM of Bi-doped rGO/Co₃O₄ nanohybrids; (d) low-magnification
192 TEM and (e) HR-TEM image of Bi-doped rGO/Co₃O₄ nanohybrids; the corresponding SEM-EDX elemental
193 mapping of the selected area (f - i).

194

195 Fig. 2 shows the crystalline phases of undoped rGO/Co₃O₄ (0%BGCO) composite
196 and Bi-doped rGO/Co₃O₄ nanohybrids obtained using the XRD. The diffraction peaks
197 of rGO/Co₃O₄ (0%BGCO) composite and Bi-doped rGO/Co₃O₄ including 1%BGCO,
198 3%BGCO, and 6%BGCO nanohybrids are the same with those of the cubic Co₃O₄
199 (JCPDS No. 43-1003). Due to the tiny doping amount of Bi sources in the preparation
200 of Bi-doped rGO/Co₃O₄ nanocomposite, no obviously crystalline phases corresponding
201 to the Bi or Bi compound such as Bi₂O₃ appeared in 1%BGCO, 3%BGCO, and
202 6%BGCO, which indicates that Bi doping did not obviously change the cubic structure
203 of Co₃O₄ (or that there are present below the minimum detection limit of XRD
204 diffraction). On the other hand, the Bi₂O₃ crystalline phase can be identified if the

205 doping amount of Bi is 10% in the 10%BGCO system (see Fig. S1, supporting
206 information). Additionally, the diffraction peaks are sharp and strong, manifesting the
207 good crystallinity and relatively small particle sizes, which are beneficial for the sensing
208 performance [29].

209

210 **Fig. 2.** XRD patterns of 0%BGCO composite and BGCO nanohybrids of 1%BGCO, 3%BGCO and 6%BGCO.

211

212 Fig. 3a shows the high resolution XPS spectrum of C 1s, which indicates a high level
213 oxidation of the graphene sheets, occurred during the exfoliation. There are three peaks
214 with their binding energies at 284.2 eV, 286.1 eV and 289.7 eV, respectively, which can
215 be assigned to the aromatic carbon (C-C), the epoxy or alkoxy (C-O) and the carbonyl
216 carbon (C=O), respectively. Fig. 3b shows the deconvoluted O 1s spectrum of Bi-doped
217 rGO/Co₃O₄ composites. The two peaks centered at 529.7 and 531.6 eV are attributed to
218 the O²⁻ lattice oxygen, and chemisorbed oxygen species such as (O⁻, O₂⁻ and O²⁻),
219 respectively, leading to the formation of electron depletion layer within the matrix of
220 1%BGCO [44,45]. Fig. 3c shows the binding energies of Co 2p_{1/2} and Co 2p_{3/2} in Co
221 2p XPS spectra, which are located at 794.5 eV and 779.86 eV, respectively. The
222 difference between these two binding energy values is ~14.6 eV, suggesting that both
223 Co³⁺ and Co²⁺ are co-existed in the nanohybrids of 1%BGCO [46,8]. Moreover, the
224 other two satellite peaks located at 796.6 eV and 781.6 eV are linked to the Co²⁺ peak
225 of two orbits [47]. Fig. 3d shows Bi 4f spectrum, and the binding energies for Bi 4f_{5/2}
226 and Bi 4f_{7/2} are 164.90 and 159.56 eV, respectively. These show that all of the Bi species
227 in the 1%BGCO sample are in the form of Bi³⁺, which agrees well with the previous
228 reports [1,48]. Additionally, the high resolution XPS spectra of other three samples of
229 0%BGCO, 3%BGCO, and 6%BGCO were analyzed, revealing that the samples surface
230 is composed of the elements of Co, C, O and Bi, in which Bi acts as a decorating
231 component (see Fig. S2 to 4, supporting information).

232

233 **Fig. 3.** XPS spectra of Bi-doped rGO/Co₃O₄ nanocomposites: (a) C 1s, (b) O 1s, (c) Co 2p and (d) Bi 4f, respectively.

234

235 Most of semiconductor-based sensors show temperature-dependent characteristics
236 due to their unique electrical structures, which are strongly affected by temperature
237 [49,50]. Thus, the different gas sensors have their individual optimum working
238 temperatures. This is beneficial for improving the sensitivity and/or the selectivity
239 according to the equation (1):

$$240 \quad n_0 = 2(m_n^* k_0 T / 2\pi \hbar)^{3/2} \exp(-(E_c - E_f) / k_0 T) \quad (1) [1]$$

241 where T is Kelvin temperature scale, m_n^* is effective mass, k_0 is the Boltzmann
242 constant, \hbar is reduced Planck constant, E_c is the energy of conduction band bottom and
243 E_f is the energy of Fermi level. We firstly tried to find the optimum operating
244 temperature of the developed sensor. Fig. 4 shows the results of the sensing responses
245 versus operating temperature (T) of the 0%BGCO and Bi-doped rGO/Co₃O₄
246 nanohybrids based sensor to 100 ppm ethanol. Through comparisons of the temperature
247 dependent sensing characteristics in the temperature range of 80 - 200 °C, we found that
248 the sensors of the 0%BGCO, 1%BGCO, 3%BGCO and 6%BGCO exhibit their
249 optimum sensing properties at temperatures of 150 °C, 120 °C, 130 °C, and 140 °C,
250 respectively. Obviously, the sensor of 1%BGCO exhibits the outstanding sensing
251 performance among all the sensors, and its optimum working temperature is 120 °C.

252

253 **Fig. 4.** Sensing performances of the gas sensors toward 100 ppm ethanol gas at different operating temperatures.

254

255 To further reveal the changing trend of resistance (R_a) for the different BGCO sensors,
256 the relationship curves between R_a values and the proportion of Bi dopant at different
257 operating temperature from 80 to 200 °C were obtained, and the results are shown in
258 Fig. 5a. Obviously, the resistance values of 1%BGCO, 3%BGCO and 6%BGCO
259 increase with the increase of Bi content in the BGCO nanohybrids at the same
260 temperature, which indicates that the introduction of Bi element has significantly
261 influenced the sensor's responses. The main reason can be ascribed to the fact that with
262 a higher Bi content, the energy barrier and scattering cross-section could be increased,
263 which would prevent the effective charge-transfer [51]. Additionally, the device's
264 resistance decreases with the increase of the operating temperature, which is the

265 intrinsic characteristic of all the MOSCs. Furthermore, we also found that the resistance
266 of 0%BGCO is the largest one among the samples of 1%BGCO, 3%BGCO and
267 6%BGCO. This phenomenon is in a good agreement with that reported in literature
268 [39,52].

269 Fig. 5b exhibits the dynamic response and recovery characteristics of the sensors
270 based on 1%BGCO and 0%BGCO to different ethanol concentrations from 500 ppb to
271 500 ppm tested at 120 °C. Obviously, the dynamic curves display a slow increase at a
272 low ethanol concentration below 5 ppm. Afterwards the responses increase quickly after
273 5 ppm. In general, the 1%BGCO sensor exhibits much a higher response than that of
274 0%BGCO, which is mainly due to its increased content of Bi elements. Furthermore,
275 the response of 1%BGCO sensor increases rapidly with the increasing concentration of
276 ethanol, which can reach 178.1 at the ethanol concentration of 500 ppm. By taking the
277 logarithm of R_a of samples of 0%BGCO and 1%BGCO, we found that the R_a of
278 1%BGCO exhibits a significant change with the increase of ethanol concentration, see
279 Fig. 5c. On the other hand, it is worth mentioning that the R_a values of 1%BGCO,
280 3%BGCO, and 6%BGCO based sensors are much lower than that of 0%BGCO sensor
281 due to the incorporation of Bi dopant, as shown in Fig 5d. Moreover, the resistance (R_a)
282 of all the sensors can return to the baseline level (see Fig. 5d) which manifest that the
283 BGCO materials have excellent recovery property when exposed to fresh air again from
284 the target gas of ethanol. The detailed response and recovery performance will be
285 discussed in the following section of this study. For comparisons, the dynamic response
286 and recovery curves of the sensors based on 3%BGCO and 6%BGCO are given in Figs.
287 S4 and S5 (Supporting Information). Clearly, the response of 1%BGCO is 6.35, which
288 is ~ 8.17 times as large as those of 3%BGCO and 6%BGCO, respectively. Furthermore,
289 the response of 1%BGCO is gradually reaching to the saturation stage when the ethanol
290 concentration is above 200 ppm, as shown in Fig. 5e. Table 1 summarizes the sensing
291 data of ethanol using the 1%BGCO and 0%BGCO. According to the data in the table,
292 the 1%BGCO sensor shows a superior response than that of 0%BGCO sensor, mainly
293 because of its larger specific surface area (67.795 m²/g) and incorporation of Bi
294 elements.

295

296

297 **Table 1** The response data of 1%BGCO and 0%BGCO based sensors toward 100 ppm ethanol at 120 °C.

Materials	Concentrations (unit: ppm)							
	0.5	1	5	20	50	100	200	500
1%BGCO	2.5	8.2	15.0	59.8	104.6	136.7	157.6	178.1
0%BGCO	1.2	1.2	1.4	1.6	1.7	2.0	2.2	2.4

298

299 Fig. 5f shows a typical repeatable sensing results of the 1%BGCO and 0%BGCO
300 sensors after five cycles to 100 ppm of ethanol at 120 °C. It is indicated that both the
301 1%BGCO and 0%BGCO sensors show a good reproducibility after the cycling test,
302 manifesting their good stabilities. However, the 0%BGCO sensor has only a very low
303 sensitivity of 2.0 (see Table 1). Similarly, the cycling test results of dynamic responses
304 of 3%BGCO and 6%BGCO to 100 ppm ethanol at 120 °C were also studied, and the
305 results are shown in Figs. S6 and S7 (Supporting Information). Based on all these
306 results, we can conclude that the introduction of Bi can significantly enhance the
307 sensitivity of the rGO/Co₃O₄ composite, meanwhile, the repeatability and stability of
308 Bi-doped rGO/Co₃O₄ nanohybrids are well maintained.

309

310 **Table 2** Gas sensing response values of various nanomaterials to ethanol gas.

Materials	Concn (ppm)	Temp (°C)	Response	Refs.
TiO ₂ /Co ₃ O ₄	100	160	65	[53]
ZnO-Co ₃ O ₄	1000	200	106	[54]
Co ₃ O ₄ /Al ₂ O ₃	50	240	8.9	[55]
Pd@Co ₃ O ₄ -ZnO	200	240	59	[56]
α -Bi ₂ Mo ₃ O ₁₂ / Co ₃ O ₄	100	170	30.25	[57]
rGO/CoTiO ₃	50	195	9	[58]
Co ₃ O ₄ /N-doped carbon foam	100	100	10.4	[59]
3 wt% rGO-Co ₃ O ₄	100	180	13.5	[35]
rGO/Co ₃ O ₄	100	200	21	[7]
Co ₃ O ₄ /N-RGO-0.5	100	200	24.5	[8]
1%BGCO	100	120	150	This work

311

312

313

314

315 **Fig. 5.** (a) The initial resistance alteration trend of the Bi-doped rGO/Co₃O₄ (BGCO) nanohybrids induced by the
316 proportion of Bi dopant at the different temperature from 80 to 200 °C; (b) Dynamic resistance changes of the
317 0%BGCO and 1%BGCO sensors when exposed to various ethanol gas toward 0.5-500 ppm ethanol at 120 °C,
318 respectively; (c) Continuous resistance curves of the 0%BGCO and 1%BGCO sensors to various concentrations of
319 ethanol at 120 °C; (d) The initial resistances (R_a) of the 0%BGCO, 1%BGCO, 3%BGCO and 6%BGCO sensors
320 varied with the ethanol concentration at 120 °C, respectively; (e) The response *vs* gas concentrations for 0%BGCO
321 and 1%BGCO sensors, respectively; (f) Repeatability test of the 0%BGCO and 1%BGCO nanocomposite sensors
322 to 100 ppm of ethanol at 120 °C.

323

324 Figs. 6a and b compare the response and recovery times of the 1%BGCO sensor and
325 0%BGCO sensor exposed to 100 ppm ethanol at 120 °C. The τ_{res} of 0%BGCO sensor
326 is 5 s, which is faster than that (89 s) of 1%BGCO sensor. On the other hand, both the
327 sensors take a long time to recover 90% of its initial resistance, especially for the
328 1%BGCO (75 s). Most of the chemical sensors do not show good reversibility because
329 the thermal energy is usually lower than the activation energy for desorption [60], which
330 leads to a long τ_{rec} . In addition, the gas sensor based on the rGO and its hybrids exhibits
331 a much longer recovery time, which has often been reported in literature [61,62]. The
332 main reason is attributed to the lamellar structure of rGO and mesoporous structures in
333 1%BGCO, which cause the slow diffusion of the ethanol molecules.

334 The long-term stability is also a very important parameter for gas sensors, thus the
335 sensing stability of 1%BGCO and 0%BGCO exposed to 100 ppm ethanol was studied
336 once per 10 days at 120 °C for a period of two months to evaluate their long-term stable
337 performance. After two months, the 1%BGCO sensor still maintains 92% of the initial
338 value with a good stability, but no clear change of the 0%BGCO because of its low
339 sensitivity (Fig. 6c).

340 It is practical to investigate the sensing performance of the sensors at differently
341 humid conditions because the humidity could greatly deteriorate the sensing property
342 of gas sensors. This has been investigated and the obtained results are shown in Fig. 6d.

343 The responses are maintained at around 150 in the relative humidity range of 30-50 %,
344 but then decreases gradually with the further increase of the relative humidity. The
345 response can still retain at 101.8 when exposed to 100 ppm of ethanol as the relative
346 humidity reaches to 80 %, indicating that the 1%BGCO sensor can work at a relatively
347 high humidity up to 80% for the detection of ethanol.

348

349 **Fig. 6.** (a) and (b) Dynamic resistance curves of the 0%BGCO and 1%BGCO sensors toward 100 ppm ethanol at
350 120 °C; (c) Response stability of 0%BGCO and 1%BGCO sensors toward ethanol at 120 °C lasting for 10, 20, 30,
351 40, 50, and 60 days; (d) sensing performances of 0%BGCO and 1%BGCO sensors at different humidity with a
352 concentration of 100 ppm ethanol gas 120 °C.

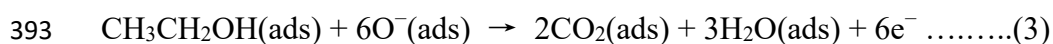
353

354 The selectivity and cross-responses of 0%BGCO and 1%BGCO sensors to different
355 gases (all with a volume of 100 ppm) including acetone (C_2H_6CO), isopropanol
356 ($(CH_3)_2CHOH$), benzene ($C_6H_5CH_3$), ammonia (NH_3), trimethylamine (C_3H_9N) and
357 NO_2 were tested at 120 °C. The obtained results are shown in Fig. 7a, which clearly
358 indicates that the gas sensors are more sensitive to ethanol than the other gases as well
359 as oxidizing gas of NO_2 , especially for 1%BGCO sensor (Fig. 7a). According to the
360 literature [63], the incorporation of Bi dopant can promote the redox reaction, whereas
361 the MOSCs can act as the catalyst. Therefore, the incorporation of Bi in BGCO provides
362 the obtained sensing material with a superior catalytic selectivity for the redox reaction
363 between chemisorbed oxygen and ethanol molecules.

364 It is well-known that gas sensing performance is related to surface chemisorption and
365 catalytic reaction. The sensing mechanism based on the changes of conductivity is
366 mainly originated from the interaction between the adsorbed gaseous molecules and
367 sensing materials as well as the reactions between the absorbed target molecules and
368 oxygen molecules on the surface of sensing material. Therefore, the sensing
369 performance of MOSCs is closely related to their composition, electronic structure,
370 crystallinity and crystal size, as well as surface morphology, which significantly affect
371 their capacities of adsorbing target gas and oxygen ions on the surface. When the
372 1%BGCO sensor are exposed to air, oxygen molecules (O_2) will be chemically

373 adsorbed onto the surface of the sensing materials to form oxygen ions (O^-) through
 374 binding free hot electrons from the conductance band (E_c) of 1%BGCO nano hybrids.
 375 The rGO nanosheets has a high electron mobility (μ), and could act as a medium to
 376 accept electrons. This facilitates the migration of carriers during the catalytic process,
 377 thus promoting the enhancement of sensing performances [31,32]. In this 1%BGCO
 378 nano hybrids system, when the sensing material was exposed to ethanol vapor gas, the
 379 ethanol molecules (CH_3CH_2OH) can react with the adsorbed oxygen species on the
 380 surface. Thereafter, the electrons are released back to the E_c and thereby the sensor
 381 resistance is increased greatly.

382 To further study the electron transfer behavior in the 1%BGCO nano hybrid system,
 383 UPS analysis was carried out. As shown in Fig. 7b, the cut off energy of 1%BGCO
 384 nano hybrids is 16.93 eV, indicating that the work function of the 1%BGCO
 385 nano hybrids is 4.27 eV, which facilitates the transportation of electrons [64]. On the
 386 other hand, when the Bi-doped rGO/ Co_3O_4 nano hybrids are formed, conduction
 387 electrons of Bi-doped rGO grains are obtained from Co_3O_4 (if holes, to follow the
 388 opposite direction) to balance Fermi level (E_f), thus forming an electron depletion layer
 389 (EDL) at the interface Bi-doped rGO/ Co_3O_4 and consequently increasing the R_a ,
 390 according to the energy band diagram as schematically illustrated in Figs. 7c and d. The
 391 processes can be expressed using the following two reactions (2) and (3): [65].



394
 395

396 **Fig. 7.** (a) The selectivity of the sensors based on 0%BGCO and 1%BGCO to different gases with a concentration
 397 of 100 ppm at 120 °C; (b) UPS spectrum of 1%BGCO nano hybrids; (c) the energy band structure before contact of
 398 rGO and Co_3O_4 and (d) the energy band structure after contact of rGO and Co_3O_4 .

399

400 **4. Conclusions**

401 In summary, the Bi-doped rGO/ Co_3O_4 (BGCO) nano hybrids have been rationally
 402 designed and successfully synthesized via one-step solvothermal process, and their

403 ethanol-sensing performances were investigated. Specifically, the 1%BGCO sensor
404 shows the superior sensing response of 150 at 120 °C towards 100 ppm ethanol, a low
405 detection limit (500 ppb). Moreover, the BGCO sensor shows excellent selectivity to
406 ethanol compared to other organic volatile gases. The excellent gas sensing
407 performance of 1%BGCO is mainly attributed to the appropriate content Bi and
408 synergistic effect between Bi and rGO/Co₃O₄ system. Additionally, incorporation of Bi
409 dopant can promote the redox reaction, whereas the MOSCs act as the catalyst. Thus,
410 this study provides a new strategy for using the Bi-doped rGO/Co₃O₄ for ethanol
411 sensing.

412

413 **Acknowledgements**

414 This work was financially supported by the National Natural Science Foundation of
415 China (Grant No. 51227804). This work was also funded by the Postdoctoral Scientific
416 Research Foundation of Qingdao, National College Students Innovation and
417 Entrepreneurship Training Program of China (No. G201911065028), College Students
418 Innovation and Entrepreneurship Training Program of Qingdao University
419 (X201911065058). The authors would like to thank the Chemical Experimental
420 Teaching Center of Qingdao University for the characterizations, and Kehui Han from
421 Shiyanjia Lab (www.shiyanjia.com) for the XPS and UPS analysis.

422

423 **Conflicts of interest**

424 There are no conflicts to declare

425 **Note**

426 † These two authors contribute equally

427

428

429

430

431

432

433 **References**

434 [1] P. Wang, S.Z. Wang, Y.R. Kang, Z.S. Sun, X.D. Wang, Y. Meng, M.H. Hong, W.F.
435 Xie, Cauliflower-shaped Bi₂O₃–ZnO heterojunction with superior sensing performance
436 towards ethanol, *J. Alloys Compd.* 854 (2021), 157152.

437 [2] X.Y. Tian, Z.Y. Liu, Z.W. Luo, X. Wu, F. Qiao, X.W. Wang, G.H. Li, J. Wu, J. Zhang,
438 Z. Liu, J.H. Chu, Dual-mode sensor and actuator to learn human-hand tracking and
439 grasping, *IEEE Trans. Electron Devices* 66 (2019) 5407–5410.

440 [3] Z.W. Luo, X.T. Hu, X.Y. Tian, C. Luo, H.J. Xu, Q.L. Li, Q.H. Li, J. Zhang, F. Qiao,
441 X. Wu, V.E. Borisenko, J.H. Chu, Structure-property relationships in graphene-based
442 strain and pressure sensors for potential artificial intelligence applications, *Sensors* 19
443 (2019), 1250

444 [4] J. Walker, P. Karnati, D.R. Miller, M. Al-Hashem, S.A. Akbar, P.A. Morris, A new
445 open-access online database for resistive-type gas sensor properties and performance,
446 *Sens. Actuators B Chem.* 321 (2020), 128591.

447 [5] P. Srinivasan, A.J. Kulandaisamy, G.K. Mani, K.J. Babu, K. Tsuchiya, J.B.B.
448 Rayappan, Development of an acetone sensor using nanostructured Co₃O₄ thin films
449 for exhaled breath analysis, *RSC Adv.* 9 (2019) 30226–30239.

450 [6] F. Xing, S. Zhang, Y. Yang, W.S. Jiang, Z.B. Liu, S.W. Zhu, X.C. Yuan, Chemically
451 modified graphene films for high-performance optical NO₂ sensors, *Analyst* 141 (2016)
452 4725-4732.

453 [7] M.H. Tian, J.Y. Miao, P.F. Cheng, H.C. Mu, J.C. Tu, J.B. Sun, Layer-by-layer
454 nanocomposites consisting of Co₃O₄ and reduced graphene (rGO) nanosheets for high
455 selectivity ethanol gas sensors, *Appl. Surf. Sci.* 479 (2019) 601–607.

456 [8] G. Lin, H. Wang, X.Y. Lai, R.S. Yang, Y.Z. Zou, J.W. Wan, D. Liu, H. Jiang, Y. Hu,
457 Co₃O₄ /N-doped RGO nanocomposites derived from MOFs and their highly enhanced
458 gas sensing performance, *Sens. Actuators B Chem.* 303 (2020), 127219

459 [9] P.V. Shinde, N.M. Shinde, S.F. Shaikh, D. Lee, J.M. Yun, L.J. Woo, A.M. Al-Enizi,
460 R.S. Mane, K.H. Kim, Room-temperature synthesis and CO₂-gas sensitivity of bismuth
461 oxide nanosensors, *RSC Adv.* 10 (2020) 17217–17227.

462 [10] K. Kim, P.G. Choi, T. Itoh, Y. Masuda, Catalyst-free highly sensitive SnO₂
463 nanosheet gas sensors for parts per billion-level detection of acetone, ACS Appl. Mater.
464 Interfaces 12 (2020) 51637–51644.

465 [11] F.H. Zhang, Y.C. Wang, L. Wang, J. Liu, H.L. Ge, B. Wang, X.Y. Huang, X.D.
466 Wang, Z.T. Chi, W.F. Xie, High performance In₂(MoO₄)₃@In₂O₃ nanocomposites gas
467 sensor with long-term stability, J. Alloys Compd. 805 (2019) 180-188.

468 [12] D. Wang, L.F. Deng, H.J. Cai, J.L. Yang, L.P. Bao, Y.H. Zhu, X.Y. Wang,
469 Bimetallic PtCu nanocrystal sensitization WO₃ hollow spheres for highly efficient 3-
470 Hydroxy-2-butanone biomarker detection, ACS Appl. Mater. Interfaces 12 (2020)
471 18904–18912.

472 [13] N. Tammanoon, T. Iwamoto, T. Ueda, T. Hyodo, A. Wisitsoraat, C. Liewhiran, Y.
473 Shimizu, Synergistic Effects of PdO_x–CuO_x Loadings on Methyl Mercaptan Sensing of
474 Porous WO₃ Microspheres Prepared by Ultrasonic Spray Pyrolysis, ACS Appl. Mater.
475 Interfaces 12 (2020) 41728-41739.

476 [14] K.C. Wan, D. Wang, F. Wang, H.J. Li, J.C. Xu, X.Y. Wang, J.H. Yang, Hierarchical
477 In₂O₃@SnO₂ core–shell nanofiber for high efficiency formaldehyde detection, ACS
478 Appl. Mater. Interfaces 11 (2019) 45214–45225.

479 [15] X. Wang, M.Z. Gao, Porous Co₃O₄/SnO₂ quantum dot (QD) heterostructures with
480 abundant oxygen vacancies and Co²⁺ ions for highly efficient gas sensing and oxygen
481 evolution reaction, Nanoscale 10 (2018) 12045–12053.

482 [16] P. Wang, S.Z. Wang, Q. Han, D.Q. Zou, W.K. Zhao, X.D. Wang, C. Luo, X. Yang,
483 X. Wu, W.F. Xie, Construction of hierarchical α-Fe₂O₃/SnO₂ nanoball arrays with
484 superior acetone sensing performance, Adv. Mater. Interfaces (2020), 2001831.

485 [17] N. Devabharathi, A.M. Umarji, S. Dasgupta, Fully inkjet-printed mesoporous
486 SnO₂-based ultrasensitive gas sensors for trace amount NO₂ detection, ACS Appl.
487 Mater. Interfaces 12 (2020) 57207–57217.

488 [18] Z.J. Han, Y. Qi, Z.Y. Yang, H.C. Han, Y.Y. Jiang, W.J. Du, X. Zhang, J.Z. Zhang,
489 Z.F. Dai, L.L. Wu, C. Fletcher, Z. Wang, J.R. Liu, G.X. Lu, F.L. Wang, Recent advances
490 and perspectives on constructing metal oxide semiconductor gas sensing materials for
491 efficient formaldehyde detection, J. Mater. Chem. C 8 (2020) 13169–13188.

- 492 [19] P. Karnati, S. Akbar, P.A. Morris, Conduction mechanisms in one dimensional
493 core-shell nanostructures for gas sensing: A review, *Sens. Actuators B Chem.* 295 (2019)
494 127–143.
- 495 [20] F.B. Gu, M.Y. Di, D.M. Han, S. Hong, Z.H. Wang, Atomically dispersed Au on
496 In₂O₃ nanosheets for highly sensitive and selective detection of formaldehyde, *ACS*
497 *Sens.* 5 (2020) 2611–2619.
- 498 [21] D. Wang, Y. Yin, P.C. Xu, F. Wang, P. Wang, J.C. Xu, X.Y. Wang, X.X. Li, The
499 catalytic-induced sensing effect of triangular CeO₂ nanoflakes for enhanced BTEX
500 vapor detection with conventional ZnO gas sensors, *J. Mater. Chem. A* 8 (2020) 11188-
501 11194.
- 502 [22] H.Y. Tang, L.N. Sacco, S. Vollebregt, H.Y. Ye, X.J. Fan, G.Q. Zhang, Recent
503 advances in 2D/nanostructured metal sulfide-based gas sensors: mechanisms,
504 applications, and perspectives, *J. Mater. Chem. A* 8 (2020) 24943–24976.
- 505 [23] A. Beniwal, Sunny, SnO₂-ZnO-Fe₂O₃ tri-composite based room temperature
506 operated dual behavior ammonia and ethanol sensor for ppb level detection, *Nanoscale*
507 12 (2020) 19732–19745.
- 508 [24] Z.D. Hu, X.Y. Sun, H.F. Li, Y.R. Kang, X.Q. Song, P. Wang, Q.T. Luan, X.D. Wang,
509 Z.T. Chi, W.F. Xie, Cobalt monosulfide nanofibers: ethanol sensing and magnetic
510 properties, *Rare Metals* (2021).
- 511 [25] Q.C. Li, D. Chen, J.M. Miao, S.J. Lin, Z.X. Yu, D.X. Cui, Z. Yang, X.P. Chen,
512 Highly sensitive sensor based on ordered porous ZnO nanosheets for ethanol detecting
513 application, *Sens. Actuators B Chem.* 326 (2021), 128952.
- 514 [26] Z.J. Li, H. Li, Z.L. Wu, M.K. Wang, J.T. Luo, H. Torun, P.A. Hu, C. Yang, M.
515 Grundmann, X.T. Liu, Y.Q. Fu, Advances in designs and mechanisms of
516 semiconducting metal oxide nanostructures for high-precision gas sensors operated at
517 room temperature, *Mater. Horizons* 6 (2019) 470–506.
- 518 [27] I. Boehme, U. Weimar, N. Barsan, Unraveling the surface chemistry of CO sensing
519 with In₂O₃ based gas sensors, *Sens. Actuators B Chem.* 326 (2021), 129004.
- 520 [28] V.S. Bhati, S. Ranwa, S. Rajamani, K. Kumari, R. Raliya, P. Biswas, M. Kumar,
521 Improved sensitivity with low limit of detection of a hydrogen as sensor based on rGO-

522 loaded Ni-doped ZnO nanostructures, *ACS Appl. Mater. Interfaces* 10 (2018) 11116–
523 11124.

524 [29] L.H. Liu, M. Yang, S. Gao, X.F. Zhang, X.L. Cheng, Y.M. Xu, H. Zhao, L.H. Huo,
525 Z. Major, Co₃O₄ hollow nanosphere-decorated graphene sheets for H₂S sensing near
526 room temperature, *ACS Appl. Nano Mater.* 2 (2019) 5409–5419.

527 [30] D.F. Ma, Y.J. Su, T. Tian, H. Yin, C. Zou, T.T. Huo, N.T. Hu, Z. Yang, Y.F. Zhang,
528 Multichannel room-temperature gas sensors based on magnetic-field-aligned 3D
529 Fe₃O₄@SiO₂@reduced graphene oxide spheres, *ACS Appl. Mater. Interfaces* 12 (2020)
530 37418-37426.

531 [31] Q.Y. Li, Y. Shen, T. Li, M. Cao, F. Gu, L.J. Wang, Enhanced ethanol sensing
532 performances of hetero-assembly Zn_{1-x}Fe_xO/rGO nanocomposites, *Sens. Actuators B*
533 *Chem.* 314 (2020), 128032.

534 [32] N. Pienutsa, P. Roongruangsree, V. Seedokbuab, K. Yannawibut, C.
535 Phatoomvijitwong, S. Srinives, SnO₂-graphene composite gas sensor for a room
536 temperature detection of ethanol, *Nanotechnology* 32 (2020), 115502.

537 [33] M.A. Modenes-Junior, C.A. Zito, T.M. Perfecto, D.P. Volanti, Ethanol detection
538 using composite based on reduced graphene oxide and CuO hierarchical structure under
539 wet atmosphere, *Mater. Sci. Eng. B* 248 (2019), 114385.

540 [34] Z.L. Tang, X.C. Deng, Y. Zhang, X.D. Guo, J.Q. Yang, C.L. Zhu, J. Fan, Y.F. Shi,
541 B.J. Qing, F.Y. Fan, MoO₃ nanoflakes coupled reduced graphene oxide with enhanced
542 ethanol sensing performance and mechanism, *Sens. Actuators B Chem.* 297 (2019),
543 126730.

544 [35] X.D. Liu, J.Y. Liu, Q. Liu, R.R. Chen, H.S. Zhang, J. Yu, D.L. Song, J.Q. Li, M.L.
545 Zhang, J. Wang, Template-free synthesis of rGO decorated hollow Co₃O₄
546 nano/microspheres for ethanol gas sensor, *Ceram. Int.* 44 (2018) 21091-21098.

547 [36] S. Syed Zahirullah, P. Immanuel, S. Pravinraj, P. Fermi Hilbert Inbaraj, J. Joseph
548 Prince, Synthesis and characterization of Bi doped ZnO thin films using SILAR method
549 for ethanol sensor, *Materials Letters* 230 (2018) 1-4.

550 [37] X. Li, D. Jiang, Y. Fan, N. Zhang, C. Liu, S. Adimi, J.R. Zhou, S.P. Wen, S.P. Ruan,
551 The effects of Zr-doping on improving the sensitivity and selectivity of a one-

552 dimensional α -MoO₃-based xylene gas sensor, *Inorg. Chem. Front.* 7 (2020) 1704-1712.

553 [38] V.K. Tomer, S. Duhan, Correction: Ordered mesoporous Ag-doped TiO₂/SnO₂

554 nanocomposite based highly sensitive and selective VOC sensors, *J. Mater. Chem. A* 8

555 (2020) 20189-20190.

556 [39] Q. Yang, Q.L. Wu, Y. Liu, S.P. Luo, X.T. Wu, X.X. Zhao, H.Y. Zou, B.H. Long, W.

557 Chen, Y.J. Liao, L.X. Li, P.K. Shen, L.L. Duan, Z.W. Quan, Novel Bi-doped amorphous

558 SnO_x nanoshells for efficient electrochemical CO₂ reduction into formate at low

559 overpotentials, *Adv. Mater.* 32 (2020), 2002822.

560 [40] P. Velusamy, R. Xing, R.R. Babu, E. Elangovan, J. Viegas, S. Liu, M.Sridaran, A

561 study on formaldehyde gas sensing and optoelectronic properties of Bi-doped CdO thin

562 films deposited by an economic solution process, *Sens. Actuators B Chem.* 297 (2019)

563 126718.

564 [41] Y.Y. Jian, W.W. Hu, Z.H. Zhao, P.F. Cheng, H. Haick, M.S. Yao, W.W. Wu, Gas

565 sensors based on chemi-resistive hybrid functional nanomaterials, *Nano-Micro Letters*

566 12 (2020), 71.

567 [42] Y.F. Huang, W.C. Jiao, Z.M. Chu, G.M. Ding, M.L. Yan, X. Zhong, R.G. Wang,

568 Ultrasensitive room temperature ppb-level NO₂ gas sensors based on SnS₂/rGO

569 nanohybrids with P–N transition and optoelectronic visible light enhancement

570 performance, *J. Mater. Chem. C* 7 (2019) 8616-863625.

571 [43] J.Y. Zhang, Y. Yu, P. Wang, C. Luo, X. Wu, Z.Q. Sun, J.L. Wang, W.D. Hu, G.Z.

572 Shen, Characterization of atomic defects on the photoluminescence in two-dimensional

573 materials using transmission electron microscope, *InfoMat* 1 (2019) 85-97.

574 [44] T.J. Hsueh, S.S. Wu, Highly sensitive Co₃O₄ nanoparticles/MEMS NO₂ gas sensor

575 with the adsorption of the Au nanoparticles, *Sens. Actuators B Chem.* (2020) 129201.

576 [45] N. Jayababu, M. Poloju, J. Shruthi, M.V.R. Reddy, NiO decorated CeO₂

577 nanostructures as room temperature isopropanol gas sensors, *RSC Adv.* 9 (2019)

578 13765-13775.

579 [46] Q.X. Feng, X.G. Li, J. Wang, A.M. Gaskov, Reduced graphene oxide (rGO)

580 encapsulated Co₃O₄ composite nanofibers for highly selective ammonia sensors, *Sens.*

581 *Actuators B Chem.* 222 (2016) 864-870.

582 [47] J. Wu, Y. Yang, C.X. Zhang, H. Yu, L.C. Huang, X.T. Dong, J.X. Wang, X.L. Wang,
583 Extremely sensitive and accurate H₂S sensor at room temperature fabricated with In-
584 doped Co₃O₄ porous nanosheets, Dalton Trans. 48 (2019) 7720-7727.

585 [48] P.V. Shinde, B.G. Ghule, N.M. Shinde, Q.X. Xia, S. Shaikh, A.V. Sarode, R.S.
586 Mane, K.H. Kim, Room-temperature successive ion transfer chemical synthesis and the
587 efficient acetone gas sensor and electrochemical energy storage applications of Bi₂O₃
588 nanostructures, New J. Chem. 42 (2018) 12530-12538.

589 [49] X.J. Yang, V. Salles, Y.V. Kaneti, M.S. Liu, M. Maillard, C. Journet, X.C. Jiang, A.
590 Brioude, Fabrication of highly sensitive gas sensor based on Au functionalized WO₃
591 composite nanofibers by electrospinning, Sens. Actuators B Chem. 220 (2015) 1112-
592 1119.

593 [50] R.K. Mishra, G. Murali, T.H. Kim, J.H. Kim, Y.J. Lim, B.S. Kim, P. P. Sahayd,
594 S.H. Lee, Nanocube In₂O₃@RGO heterostructure based gas sensor for acetone and
595 formaldehyde detection, RSC Adv. 7 (2017) 38714-38724.

596 [51] W.M.A. El Roubay, A.E.A. Aboubakr, M.D. Khan, A.A. Farghali, P. Millet, N.
597 Revaprasadu, Synthesis and characterization of Bi-doped g-C₃N₄ for
598 photoelectrochemical water oxidation. Sol. Energy 211 (2020) 478-487.

599 [52] M.C. Wu, J.S. Chih, W.K. Huang, Bismuth doping effect on TiO₂ nanofibres for
600 morphological change and photocatalytic performance, CrystEngComm 16 (2014)
601 10692-10699.

602 [53] L.Q. Zhang, Z.F. Gao, C. Liu, Y.H. Zhang, Z.Q. Tu, X.P. Yang, F. Yang, Z. Wen,
603 L.P. Zhu, R. Liu, Y.F. Li, L.S. Cui, Synthesis of TiO₂ decorated Co₃O₄ acicular nanowire
604 arrays and their application as an ethanol sensor, J. Mater. Chem. A 3 (2015) 2794-
605 2801.

606 [54] Y. Xiong, W.W. Xu, Z.Y. Zhu, Q.Z. Xue, W.B. Lu, D.G. Ding, L. Zhu, ZIF-derived
607 porous ZnO-Co₃O₄ hollow polyhedrons heterostructure with highly enhanced ethanol
608 detection performance, Sens. Actuators B Chem. 253 (2017) 523-532.

609 [55] X. Wang, R.Y. Cao, S.W. Zhang, P.Y. Hou, R.X. Han, M.H. Shao, X.J. Xu,
610 Hierarchical flowerlike metal/metal oxide nanostructures derived from layered double
611 hydroxides for catalysis and gas sensing, J. Mater. Chem. A 5 (2017) 23999-24010.

612 [56] Y.J. Sun, Z.P. Wang, W.D. Wang, G. Li, P.W. Li, K. Lian, W.D. Zhang, S. Zhuiykov,
613 J. Hu, L. Chen, Electrospinning preparation of Pd@Co₃O₄-ZnO composite nanofibers
614 and their highly enhanced VOC sensing properties, Mater. Res. Bull. 109 (2019) 255–
615 264.

616 [57] S.U. Din, M.U. Haq, R. Khatoon, X. Chen, L. Li, M. Zhang, L. Zhu, A novel
617 ethanol gas sensor based on α -Bi₂Mo₃O₁₂/Co₃O₄ nanotube-decorated particles, RSC
618 Adv. 10 (2020) 21940–21953.

619 [58] J. Lu, N. Jia, L. Cheng, K.Y. Liang, J.F. Huang, J.Y. Li, rGO/CoTiO₃
620 nanocomposite with enhanced gas sensing performance at low working temperature, J.
621 Alloys Compd. 739 (2018) 227–234.

622 [59] L. Li, C. Zhang, R. Zhang, X. Gao, S. He, M. Liu, X. Li, W. Chen, 2D ultrathin
623 Co₃O₄ nanosheet array deposited on 3D carbon foam for enhanced ethanol gas sensing
624 application, Sens. Actuators B Chem. (2017) 664-672.

625 [60] A. Bag, N.E. Lee, Gas sensing with heterostructures based on two-dimensional
626 nanostructured materials: a review, J. Mater. Chem. C 7 (2019) 13367-13383.

627 [61] B. Wang, X.L. Wang, X.C. Li, Z.J. Guo, X. Zhou, Y.Q. Wu, The effects of amino
628 substituents on the enhanced ammonia sensing performance of PcCo/rGO hybrids, RSC
629 Adv. 8 (2018) 41280-41287.

630 [62] H.F. Du, G.Z. Xie, Q.P. Zhang, Enhanced room temperature NO₂ sensing
631 performance of RGO nanosheets by building RGO/SnO₂ nanocomposite system,
632 Sensors 19 (2019), 4650.

633 [63]Z.H. Tao, Y.W. Li, B. Zhang, G. Sun, J.L. Cao, Y. Wang, Bi-doped urchin-like In₂O₃
634 hollow spheres: Synthesis and improved gas sensing and visible-light photocatalytic
635 properties, Sens. Actuators B Chem. 321 (2020), 128623.

636 [64] X.Y. Kou, F.Q. Meng, K. C, T.S. Wang, P. Sun, F.M. Liu, X. Yan, Y.F. Sun, F.M. Liu, K. Shimanoe,
637 G.Y. Lu, High-performance acetone gas sensor based on Ru-doped SnO₂ nanofibers, Sens.
638 Actuators B Chem. 320 (2020),128292.

639 [65] F. Wu, Q. Li, P. Wang, H. Xia, Z. Wang, Y. Wang, M. Luo, L. Chen, F.S. Chen, J.S.
640 Miao, X.S. Chen, W. Lu, C.X. Shan, A.L. Pan, X. Wu, W.C. Ren, D. Jariwala, W.D. Hu,
641 High efficiency and fast van der Waals hetero-photodiodes with a unilateral depletion

642 region, Nat. Commun. 10 (2019), 4663.

643 **Fig. 1.** (a) Illustration of the synthesis process of flower shaped Bi-doped rGO/Co₃O₄ nano hybrids; (b) low-
644 magnification SEM and (c) high-magnification SEM of Bi-doped rGO/Co₃O₄ nano hybrids; (d) low-magnification
645 TEM and (e) HR-TEM image of Bi-doped rGO/Co₃O₄ nano hybrids; the corresponding SEM-EDX elemental
646 mapping of the selected area (f - i).

647

648

649

650 **Fig. 2.** XRD patterns of 0%BGCO composite and BGCO nano hybrids of 1%BGCO, 3%BGCO and 6%BGCO.

651

652

653

654 **Fig. 3.** XPS spectra of Bi-doped rGO/Co₃O₄ nanocomposites: (a) C 1s, (b) O 1s, (c) Co 2p and (d) Bi 4f, respectively.

655

656

657

658 **Fig. 4.** Sensing performances of the gas sensors toward 100 ppm ethanol gas at different operating temperatures.

659

660

661

662 **Fig. 5.** (a) The initial resistance alteration trend of the Bi-doped rGO/Co₃O₄ (BGCO) nano hybrids induced by the
663 proportion of Bi dopant at the different temperature from 80 to 200 °C; (b) Dynamic resistance changes of the
664 0%BGCO and 1%BGCO sensors when exposed to various ethanol gas toward 0.5-500 ppm ethanol at 120 °C,
665 respectively; (c) Continuous resistance curves of the 0%BGCO and 1%BGCO sensors to various concentrations of
666 ethanol at 120 °C; (d) The initial resistances (R_a) of the 0%BGCO, 1%BGCO, 3%BGCO and 6%BGCO sensors
667 varied with the ethanol concentration at 120 °C, respectively; (e) The response vs gas concentrations for 0%BGCO
668 and 1%BGCO sensors, respectively; (f) Repeatability test of the 0%BGCO and 1%BGCO nanocomposite sensors
669 to 100 ppm of ethanol at 120 °C.

670

671

672

673 **Fig. 6.** (a) and (b) Dynamic resistance curves of the 0%BGCO and 1%BGCO sensors toward 100 ppm ethanol at
674 120 °C; (c) Response stability of 0%BGCO and 1%BGCO sensors toward ethanol at 120 °C lasting for 10, 20, 30,
675 40, 50, and 60 days; (d) sensing performances of 0%BGCO and 1%BGCO sensors at different humidity with a

676 concentration of 100 ppm ethanol gas 120 °C.

677

678 **Fig. 7.** (a) The selectivity of the sensors based on 0%BGCO and 1%BGCO to different gases with a concentration

679 of 100 ppm at 120 °C; (b) UPS spectrum of 1%BGCO nanohybrids; (c) the energy band structure before contact of

680 rGO and Co_3O_4 and (d) the energy band structure after contact of rGO and Co_3O_4 .

681

682